Fault Rerupture during the July 2019 Ridgecrest Earthquake Pair from Joint Slip Inversion of InSAR, Optical Imagery, and GPS

Yohai Magen[*,1,2], Alon Ziv[1], Asaf Inbal[1], Gidon Baer[2], and James Hollingsworth[3]

ABSTRACT

The Ridgecrest earthquake pair ruptured a previously unknown orthogonal fault system in the eastern California shear zone. The stronger of the two, an M_w 7.1 earthquake that occurred on 6 July 2019, was preceded by an M_w 6.4 foreshock that occurred 34 hr earlier. In this study, distinct final slip distributions for the two earthquakes are obtained via joint inversion of Interferometric Synthetic Aperture Radar (InSAR), optical imagery, and Global Positioning System (GPS) measurements. Special attention is paid to the merging of dense (e.g., InSAR and optical imagery) and sparse geodetic (e.g., GPS) datasets. In addition, a new approach is introduced for data and model discretization through intermittent model- and data-space reconditioning that stabilizes the inversion, thus ensuring that small changes in the data space do not cause disproportionate large changes to the model space. Although the coseismic slip of the M_w 6.4 earthquake was complex, involving three distinct asperities distributed among an intersecting orthogonal set of faults, the coseismic slip of the M_w 7.1 earthquake was limited to the main northwest-striking fault. In addition to the M_w 7.1 earthquake, that northwest-striking fault plane also hosted one of the M_w 6.4 asperities. Slip on this coplanar foreshock asperity increased the shear stress at the future site of the M_w 7.1 hypocenter, and triggered a vigorous aftershock activity on the main northwest fault that culminated in its rupture. This, in turn, reactivated the coplanar foreshock asperity. In addition to failing twice within 34 hr, we find that the reruptured asperity slipped about six times more during the M_w 7.1 than during the M_w 6.4 earthquake. This repeated failure is indicative of an incomplete stress drop and premature rupture arrest during the M_w 6.4 foreshock, requiring an efficient frictional strengthening and emphasizing the causal link between highly rate-dependent friction, dynamic frictional restrengthening, and partial stress drop that has been observed in numerical studies of frictional sliding.

KEY POINTS

- Slip distributions for the foreshock and mainshock are obtained via inversion of multiple geodetic datasets.
- Inversion stability is acquired by intermittent model- and data-space reconditioning.
- An asperity reruptured during both events, indicating an incomplete stress drop and premature rupture arrest.

INTRODUCTION

The Ridgecrest earthquake pair consists of two strike-slip earthquakes that ruptured in the eastern California shear zone (ECSZ), just north of the Garlock fault (Fig. 1). The stronger of the two, an M_w 7.1 (hereafter, the mainshock), occurred on 6 July 2019. It was preceded by an M_w 6.4 earthquake that occurred 34 hr earlier on 4 July (hereafter, the foreshock). Together, the spatial distribution of seismicity and focal plane solutions (Ross *et al.*, 2019), and surface ruptures (Brandenberg *et al.*, 2019), indicate an orthogonal set of faults, consisting of a northwest-striking right-lateral segmented fault and northeast-striking left-lateral faults (Fig. 1). This structure was unknown prior to the Ridgecrest earthquakes, as neither the background seismicity (Lin *et al.*, 2007; Hauksson *et al.*, 2012), nor surface morphology (Jennings and Bryant, 2010) indicate its existence.

A somewhat similar conjugate earthquake pair ruptured in the Imperial Valley in 1987 (Hudnut *et al.*, 1989). The sparsity of near-fault geodetic data for these earthquakes, commonly

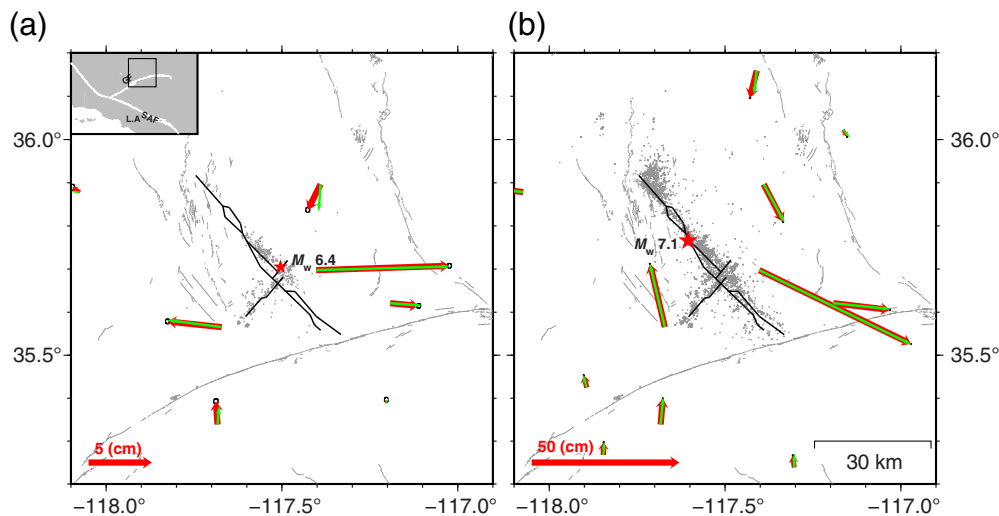*Bulletin of the Seismological Society of America* • **1627**

Figure 1. Location map and comparison between modeled (wide vectors) and observed (narrow vectors). Only a subset of Global Positioning System (GPS) offsets are shown. (a) Foreshock offsets; (b) mainshock offsets. Gray dots indicate the relocated hypocenters of earthquakes that occurred within the first 34 hr of each earthquake (Ross et al., 2019). Gray lines indicate U.S. Geological Survey mapped active faults, and black lines indicate surface traces of model faults. Inset shows a wider view of the area. GF, Garlock fault; LA, Los Angeles; SAF, San Andreas fault. The color version of this figure is available only in the electronic edition.
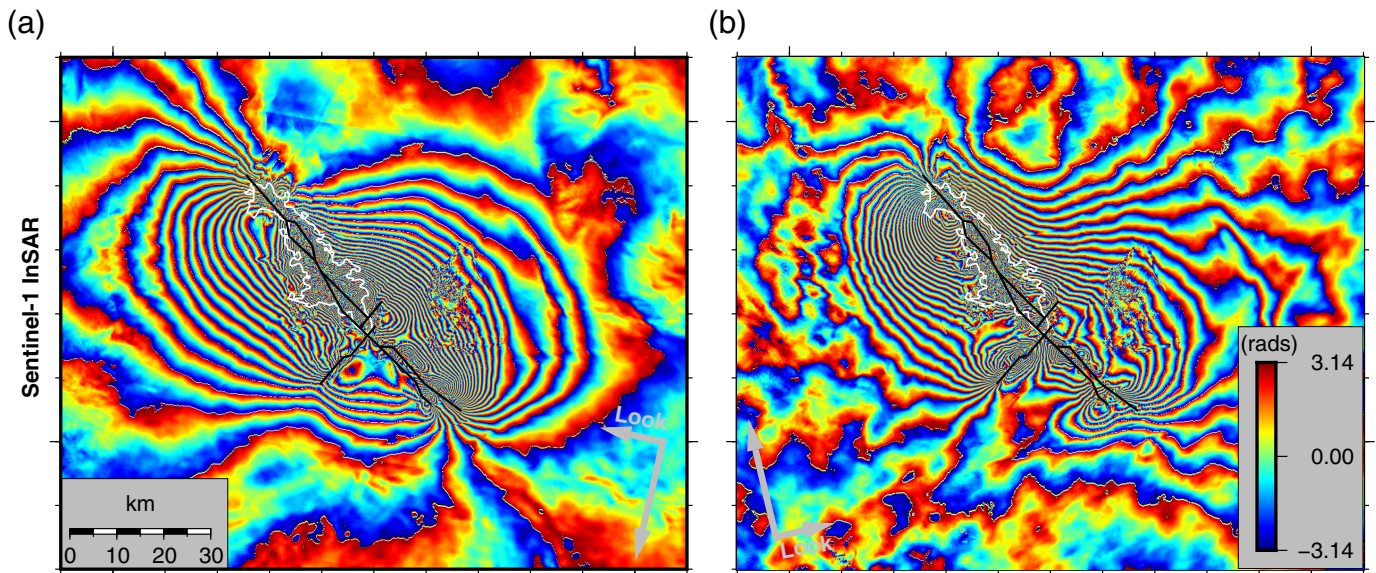
referred to as the Superstition Hills sequence, limited the resolution of the slip distribution, and hindered the investigation of coseismic fault interaction (Larsen et al., 1992). Orthogonal (or near-orthogonal) fault systems rupturing in a single event have been observed during the 1987 M_w 6.7 east Chiba (e.g., Fukuyama, 1991) and the 2008 M_w 6.9 Iwate–Miyagi Nairiku (Fukuyama, 2015) earthquakes. This has also been observed during the great 2012 M_w 8.7 Indian Ocean (e.g., Meng et al., 2012; Yue et al., 2012) and the 2018 M_w 7.9 Gulf of Alaska (e.g., Krabbenhoeft et al., 2018; Ruppert et al., 2018) intraplate oceanic earthquakes. As suggested by Fukuyama (2015), ruptures breaking orthogonal fault systems may be classified according to the timing of rupture on secondary orthogonal faults relative to the timing of rupture on the largest fault, a distinction which is important for constraining dynamic failure mechanisms. Complex events rupturing simultaneously were referred to as class A conjugate ruptures, and events rupturing sequentially were referred to as class B conjugate ruptures. Given the timing of its two largest earthquakes, the Ridgecrest pair may be classified as a class B conjugate rupture. This, however, is complicated by the fact that the M_w 6.4 foreshock broke several orthogonal faults (Ross et al., 2019). Timing of subevents composing the M_w 6.4 suggests that this event may also be classified as a class B complex rupture (Ross et al., 2019), yet the kinematic details of the M_w 6.4 foreshock are not very well resolved (Chen et al., 2020). Therefore, identifying the M_w 6.4 foreshock as a sequential conjugate rupture is contingent upon further investigation of near-fault geodetic and strong-motion data.

Notwithstanding, several other important aspects of the Ridgecrest earthquake pair clearly manifest the potential it holds

for the understanding of orthogonal fault systems. First, the quality and quantity of the geodetic and seismic datasets available for studying the slip distribution and fault interaction of the Ridgecrest pair is unprecedented, which offers a unique opportunity to observe conjugate faulting in action. Second, unlike the case with complex single-event ruptures, the time interval separating the M_w 7.1 mainshock from the M_w 6.4 foreshock is long compared to the rupture duration. This time interval, however, is several orders of magnitude shorter than the recurrence interval of $M_w \sim 6$ events in the ECSZ. This fact imposes some constraints on the state of stress around the M_w 6.4 rupture; most importantly, it rules out the possibility that the stresses acting on the foreshock slip zone reached a state comparable to the long-term state of stress. Third, the spatial proximity of the M_w 6.4 rupture to the M_w 7.1 rupture indicates that the two are related in one of two ways. Either the two ruptures are complementary (i.e., have little spatial overlap), or the two ruptures are noncomplementary; therefore, faults that slipped during the foreshock must have been reactivated by the mainshock rupture. If the two ruptures are complementary, then their space–time relations can be explained in terms of the stress field that prevailed due to the foreshock slip. If, on the other hand, the ruptures did overlap, then the foreshock stress drop must have relaxed only a fraction of the driving stresses, which implies the fault may have undergone dynamic restrengthening via a mechanism similar to the one inferred from kinematic inversions (Heaton, 1990) and friction lab experiments (e.g., Kilgore et al., 1993). A central objective of this study is to distinguish between these two alternatives.

By combining Interferometric Synthetic Aperture Radar (InSAR), optical imagery and Global Positioning System (GPS) measurements, we isolate the contribution of the foreshock to the surface displacement from that of the mainshock, and we constrain the slip distribution of the two earthquakes. Special attention is paid to the merging of dense and sparse geodetic datasets. In addition, a new approach is introduced for data and model discretization that guarantees stability, preventing small changes in the data space from causing large changes to the model space. Obtaining a robust slip distribution for each event separately also makes it possible to infer the amount of stress imparted by faults slipping during the M_w 6.4 foreshock on faults slipping during the M_w 7.1 mainshock, to assess which fault segments slipped at

(a)

(b)

Figure 2. Sentinel-1 interferograms. (a) Descending pass, 4–10 July 2019. (b) Ascending pass, 4–16 July 2019. Black lines indicate surface traces of model faults. White contour marks the spatial extent of the mainshock mask. Gray arrows indicate the flight and look directions. InSAR, Interferometric Synthetic Aperture Radar. The color version of this figure is available only in the electronic edition.

each event, and whether specific fault asperities were reactivated during the sequence of events. Finally, we discuss the mechanical implications of our observations in relation to the friction and the pulse-like rupture inferred from kinematic modeling of the mainshock (Chen *et al.*, 2020).

DATA AND PROCESSING
InSAR

We generated two Sentinel-1 interferograms in ascending and descending orbits (Fig. 2), with a maximum perpendicular baseline of 133 m. These were processed using the Gamma software (Wegmuller *et al.*, 1998) at 20 × 4 (range by azimuth) looks, resulting in pixel sizes of 45 by 56 m^2. We used the 1 arcsec National Aeronautics Space Administration's Shuttle Radar Topography Mission digital elevation model (DEM) for geocoding and topographic phase removal, and we performed phase unwrapping using the minimum cost flow algorithm (Costantini and Rosen, 1999). To reduce the interferometric phase noise and unwrapping residues, we used an adaptive filter based on the local fringe pattern (Goldstein and Werner, 1998), with a signal-to-noise ratio (SNR) threshold of 0.1. Because available InSAR images span the times of the two Ridgecrest earthquakes, additional datasets are needed to resolve the slip distribution of each earthquake separately.

Optical imagery

Critical constraints on the foreshock–mainshock slip partitioning comes from optical imagery. In this study, we used satellite imagery obtained from the planet constellation (or flock) of cubesats, which provides daily imaging at 3–5 m resolution (Fig. 3). Satellite images of the epicentral region were acquired before and after the foreshock, as well as after the mainshock; images used in our study were acquired on 27 and 30 June, and 1, 4, 6, and 12 July 2019. We use level 3B PlanetScope Ortho Scenes, which have radiometric and sensor corrections applied to the data and are subsequently orthorectified using ground-

controlled points and available DEMs (30–90 m resolution). Subpixel correlation of the various images that span the fore-shock and mainshock therefore reveals the spatial extent of surface ruptures associated with each event. Images are correlated using the Co-registration of Optically Sensed Images and Correlation software package, freely available from California Institute of Technology (e.g., Leprince *et al.*, 2007). Although the precision of correlation is much lower than InSAR (∼0.5 m for PlanetScope Ortho Scenes), the denser temporal sampling of planet imagery enables us to isolate the deformation patterns of the two events.

Limitations in the registration accuracy (especially subpixel) between images, both along-track and intertrack results in local registration (i.e., mosaicking) errors throughout the pre-, inter-, and post-earthquake orthomosaics. Although these mosaicking artifacts do not affect the offset measurements across the fault, which are relative, they do impact the long-wavelength decay of displacements away from the fault. They also limit the absolute accuracy of the displacement values. To minimize these effects, we perform a piecewise coregistration correction between along-track scenes, which involves using subpixel correlation to estimate the registration error in the region of overlap (between any two scenes), fitting a trend to the registration error, and warping one of the scenes to remove the registration error. Along-track sequences of images and neighboring image tracks can be precisely coregistered in this way. However, because of the small overlap between the scenes, stereoscopic residuals, and additional remaining distortions (likely from inaccurate rational polynomial coefficients), long-wavelength
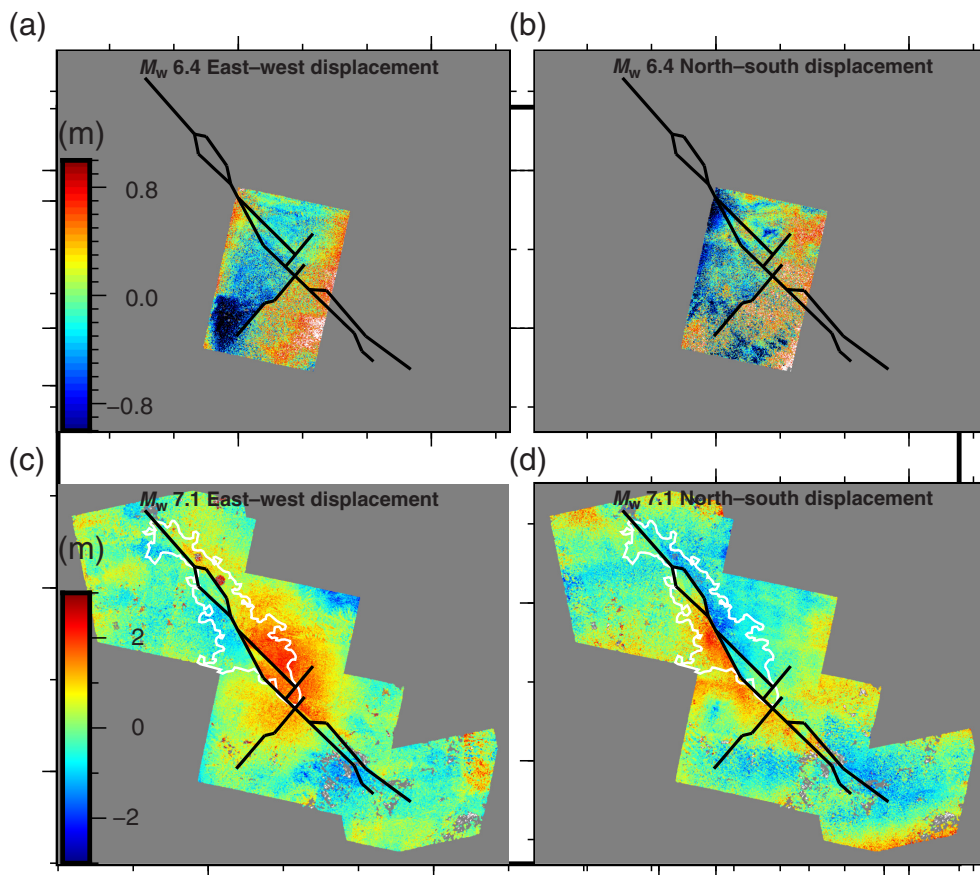
Figure 3. Planet pixel offset tracking results. Black lines mark the surface traces of model faults, and white contour marks the spatial extent of the mainshock mask. Positive values indicate east and north displacements. (a,b) Pixel offset tracking 1–4 July 2019; (c,d) pixel offset tracking between mosaic of 27 June, 30 June, and 4 July images and mosaic of 6 and 12 July images. The color version of this figure is available only in the electronic edition.

the M_w 6.4 earthquake took place on the northwest-striking fault.
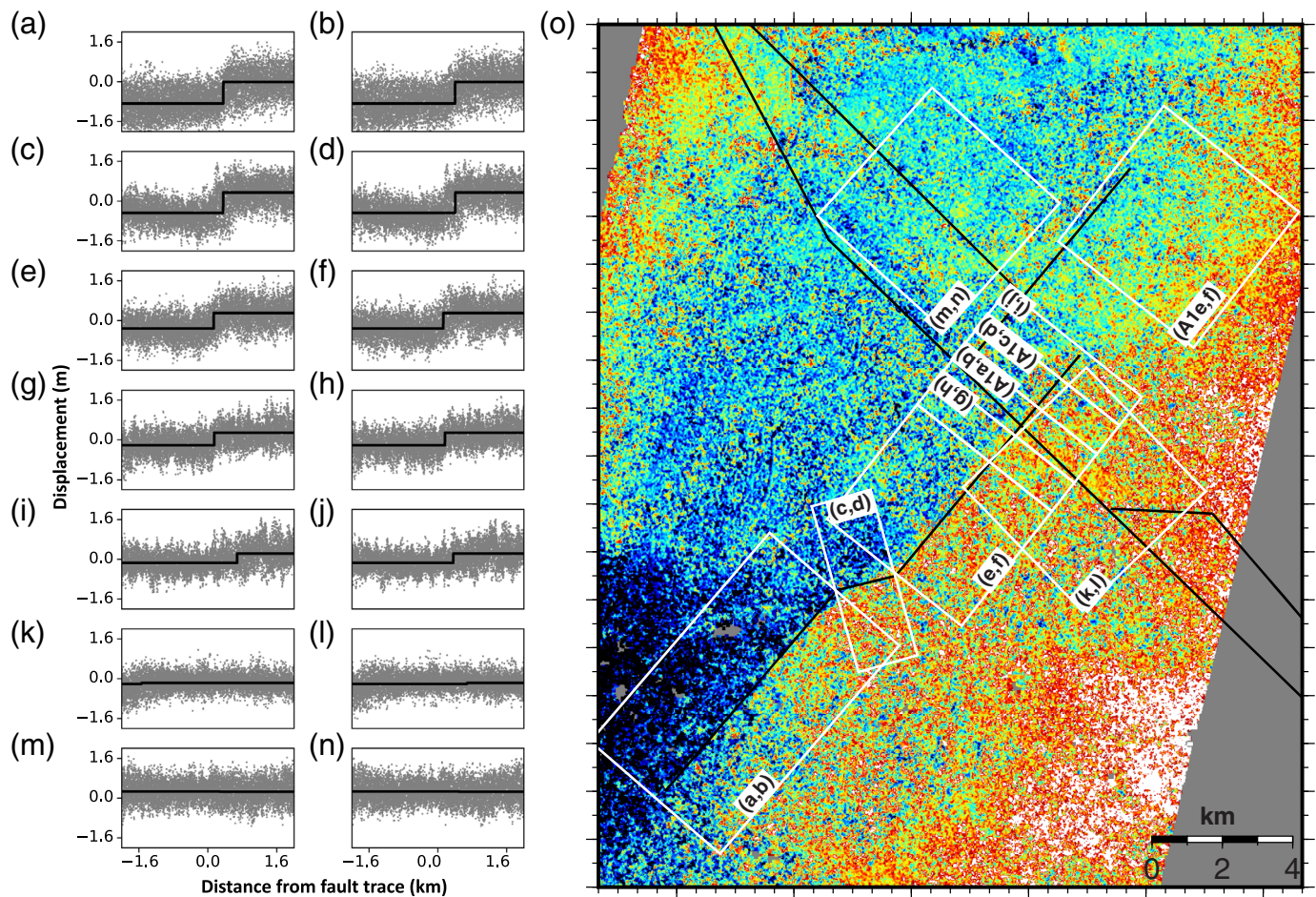
Merging of InSAR and mainshock optical imagery

A comparison between the standard deviation of the optical imagery and InSAR measurements far from the deformation signal indicates that the former is an order of magnitude noisier than the latter (Figs. 2 and 3). Thus, the use of InSAR is preferred in areas where the two datasets are available. We therefore restricted the use of the mainshock optical data to regions where the InSAR measurements are decorrelated. In reducing the optical imagery data, we followed three steps. First, we obtained InSAR coherence maps computed for a 5×5 pixels moving window. Then, because InSAR coherence (Goldstein and Werner, 1998) deteriorates rapidly below 0.2, we masked the InSAR in regions with coherence smaller than 0.2. Finally, we masked parts of the optical imagery corresponding to InSAR coherence greater than 0.2. This approach resulted in an appreciable reduction of the mainshock optical dataset, as well as its restriction to the near-fault region (see white contour in Figs. 2 and 3).

Data reduction of the foreshock optical imagery

The SNR of the foreshock optical imagery (~1.0 peak SNR) is even lower than that of the mainshock optical imagery (~2.3 peak SNR, see Fig. 3b). The only useful information that we extract from these data is a set of seven across-fault surface offsets. These are obtained by best-fitting step functions to the data within 2-kilometer-long straps, the width of which is set to be equal to the length of the near-surface dislocations (Figs. 4 and A1). The surface offset is set to be equal to the step amplitude, and its uncertainty is set to be equal to the data standard deviation within each strap on either side of the fault. Of the seven profiles along the southern part of the northeast-striking segment, six indicate east–west displacement above the noise level, and three indicate north–south displacement above that level. The offsets along the northern part of the northeast-striking fault and along the northwest-striking fault are below the noise level.

registration errors can accumulate throughout a large orthomosaic. We therefore detrend our final displacement maps using a third-order polynomial measured from the displacement field at distances of 15 + km from the rupture. We also remove outliers based on local neighborhood statistics (e.g., Zinke *et al.*, 2019).

GPS

Static surface displacements caused by the Ridgecrest's foreshock were very clearly observed at nine GPS sites located within 50 km from its epicenter. Those caused by the Ridgecrest's mainshock were very clearly observed at 19 GPS sites, located within 85 km from its epicenter (Nevada Geodetic Laboratory rapid 5 min solution, Blewitt *et al.*, 2018, see Data and Resources). Beyond those distances, GPS offsets drop significantly, and their inclusion in the dataset would have a negligible effect on the slip model. GPS offsets indicate right-lateral sense of slip on the northwest-striking segment during the M_w 7.1 earthquake, and left-lateral slip on the northeast-striking segment during the M_w 6.4 earthquake (Fig. 1). Nevertheless, these data alone cannot rule out the possibility that some slip during

Figure 4. Displacement profiles from pixel offset tracking. (a,c,e,g,i,k,m) East–west profiles; (b,d,f,h,j,l,n) north–south profiles; (o) enlarged view of the foreshock's pixel offset tracking. White rectangles enclose the subset of data used in the displacement profiles (a–n and Fig. A1a–f), with the spatial extent determined by the dimensions of the near-surface model fault dislocations. Black lines are least-square fits to a step function. They indicate a maximum of 1.2 m offset on the northeast-striking fault and no surface offsets (above the noise level) on the northwest (NW)-striking fault. The color version of this figure is available only in the electronic edition.

METHODOLOGY
Joint inversion of dense and sparse datasets

Resolving distinct slip distributions for the foreshock and main-shock is made difficult by the spatial and temporal proximity of the two earthquakes. Owing to their spatial proximity, the defor-mation field caused by one earthquake is distorted by that of the other. This distortion is further enhanced by the orthogonality of the two fault sets because in some regions the ground displace-ments associated with the two earthquakes point to the same direction, whereas in others they point in opposite directions. Joint inversion of various geodetic datasets is key for addressing these challenges. When solving for slip distribution using a composite dataset of InSAR, optical imagery, and GPS, it is sen-sible to distinguish sparse from dense datasets, and to weight them differently. In this study, the sparse dataset includes eight and 17 GPS measurements for the foreshock and mainshock, respectively, and nine along-fault optical imagery offset measure-ments enclosing the time of the foreshock. The dense dataset consists of nonoverlapping InSAR and optical imagery, with the former including the combined foreshock and mainshock displacements (and some postseismic deformation) and the latter enclosing the time of the mainshock. The following linear rela-tion is used to solve for the two slip distributions simultaneously:

$$\mathbf{Am} = \mathbf{d}, \tag{1}$$

with

$$\mathbf{A} = \begin{pmatrix} \alpha \mathbf{W}_{fs}^{GPS}\mathbf{G}_{fs}^{GPS} & 0 \\ 0 & \alpha \mathbf{W}_{ms}^{GPS}\mathbf{G}_{ms}^{GPS} \\ \alpha \mathbf{W}_{fs}^{optic}\mathbf{C}_{fs}^{optic} & 0 \\ 0 & \mathbf{W}_{ms}^{optic}\mathbf{G}_{ms}^{optic} \\ \mathbf{W}^{SAR}\mathbf{G}^{SAR} & \mathbf{W}^{SAR}\mathbf{G}^{SAR} \\ \beta\nabla & \beta\nabla \end{pmatrix}, \quad \mathbf{m} = \begin{pmatrix} m_{ms} \\ m_{fs} \end{pmatrix}, \quad \text{and}$$

$$\mathbf{d} = \begin{pmatrix} \alpha \mathbf{W}_{fs}^{GPS} d_{fs}^{GPS} \\ \alpha \mathbf{W}_{ms}^{GPS} d_{ms}^{GPS} \\ \alpha \mathbf{W}_{fs}^{optic} d_{fs}^{optic} \\ \mathbf{W}_{ms}^{optic} d_{ms}^{optic} \\ \mathbf{W}^{SAR} d^{SAR} \end{pmatrix}.$$

Explanatory notes are as follows:

1. **m** and **d** are the model and data vectors, respectively, and *A* is the model matrix.
2. The subscripts "fs" and "ms" signify the foreshock and mainshock, respectively.
3. The superscripts indicate the type of data.
4. Delta is a smoothing operator. In this study, we use a first-order spatial derivative.
5. The *G*s are the elastic kernels, relating slip on a rectangular dislocation with ground displacement (Okada, 1985).
6. The $\mathbf{C}_{fs}^{optic}$ is a matrix consisting of 0 and 1 elements, specifying (with a 1 entry) the subset of near-surface fault dislocations subject to optical imagery constraint.
7. The weights of the various datasets are determined by α and *W*, with the former being a coefficient that weighs the sparse datasets with respect to the dense ones (Fig. 5) and the latter being diagonal matrices that weigh each data point according to data-specific quality criteria.
8. Recall that the structure of $\mathbf{G}^{SAR}$ is determined automatically by the discretization algorithm (in which SAR denotes Synthetic Aperture Radar), in a manner that minimizes the condition number (CN). That algorithm operates solely on $\mathbf{G}^{SAR}$, discounting the important issue of data quality. That would not be a problem if all InSAR pixels were valid, or if the spatial distribution of invalid pixels was uniform. Because, however, InSAR data quality is far from being spatially uniform and is particularly poor near the fault trace, InSAR data points are weighted proportionally to the fraction of coherent pixels represented by that point. In this study, thanks to the high coherence of the Sentinel-1 data and the masking of the near-fault region in favor of the optical images, the $\mathbf{W}^{SAR}$ coefficients are very close to 1.
9. Each of the sparse data points (GPS and across-fault surface offsets that we obtain from the foreshock optical imagery) is weighted proportionally to its formal uncertainty (Simons *et al.*, 2002).
10. Because the optic imagery dataset is an order of magnitude noisier than the InSAR data, it is first downweighted uniformly by a factor of 10 and then weighted proportionally to the fraction of valid pixels (as the InSAR data).
11. The α coefficient is determined in two steps. First, the L2 norm of the observed-versus-modeled discrepancy of the dense dataset is plotted against the same L2 norm corresponding to the sparse dataset for different values of α. This results in an L-shaped curve, indicating a trade-off between the L2 norms of the two datasets. Then, the preferred value for α is chosen by identifying the point along that trade-off curve, the slope of which is equal to one (Fig. 5).

Finally, we adopt the fault geometry of Ross *et al.* (2019) and obtained foreshock and mainshock slip distributions by
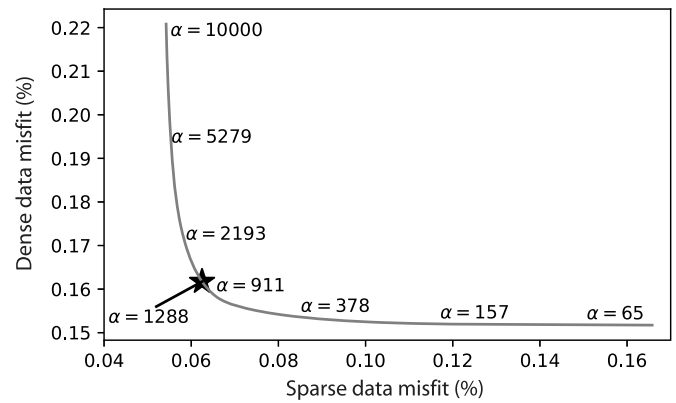

Figure 5. Dense data misfit versus sparse data misfit for different values of α, the coefficient that weighs the sparse datasets with respect to the dense ones (equation 1). Dense data refers to the InSAR measurements and optical pixel offsets, whereas the sparse data refers to the GPS measurements and the across-fault surface offsets inferred from pixel offset profiles in Figure 4. The star indicates the preferred α coefficient. CN, condition number. The color version of this figure is available only in the electronic edition.

minimizing the L2 norm of the difference between the right and left sides of equation (1), subject to a nonnegativity constraint as follows (Lawson and Hanson, 1974):

$$\min \|\mathbf{Am} - \mathbf{d}\|, \quad \mathbf{m} \geq 0. \qquad (2)$$

Reconditioning via intermittent data- and model-space discretization

The slip model is only trustworthy if it is well resolved and stable. The resolution of a solution is obtained via singular value decomposition of *A* into $U\Sigma V^T$, with *U* and *V* being orthonormal matrices that span the data and model spaces, respectively, and Σ being a diagonal matrix of singular values. The model resolution matrix is then:

$$R = UV\Sigma V^T A = A^{-g}A, \qquad (3)$$

in which A^{-g} is the generalized inverse of *A*. The resolution is perfect when *R* is equal to unity. The resolution matrix of an inverse problem may be very close to unity, and yet the inversion may be highly unstable, with small changes in the data that cause large changes in the model (Ziv, 2016). Errors in the data are mapped to the model space by the generalized inverse of the elastic kernel:

$$m_{err} = A^{-g}d_{err} = V\Sigma^{-1}U^T d_{err}. \qquad (4)$$

Thus, small singular values result in large errors in the model space, due to small errors in the data space. The sensitivity of the solution to small changes in the data may be quantified using the CN of *A* (Curtis and Snieder, 1997):

$$CN = \frac{\sigma_1}{\sigma_n}, \qquad (5)$$

with n being the dimension of A, and $\sigma_1 \geq \ldots \geq \sigma_n > 0$ being its singular values, that is, the diagonal elements of Σ. The inverse problem is stable if the CN is small. The model resolution, R, and the stability of the inverse problem, the CN, are completely determined by the properties of the matrix A, the structure of which is determined by the discretization of the data and model spaces. Thus, the ways in which the data is downsampled and the model is discretized are of great importance. Furthermore, unless the inverse problem is well conditioned, slip inversions cannot reveal the actual fault-slip distribution (Page et al., 2009; Gallovic and Ampuero, 2015; Ziv, 2016).

Ziv (2016) introduced an approach that seeks to minimize CN through data discretization. It begins with a predetermined model space and a sparse uniform data grid. It then densifies the data-space iteratively by dividing data cells into quadrants, in a manner that minimizes the CN. Although this approach does not explicitly address the resolution issue, it results in a model resolution matrix that is close to unity. In this study, building on the data resampling approach of Ziv (2016), we present a new CN-based algorithm that combines both model discretization and data downsampling. Its advantage with respect to the data-only reconditioning is that it further minimizes the CN and thus results in a more stable slip distribution. The intermittent data- and model-space discretization algorithm progresses along the following steps:

1. Initialization
   a. Set a model fault geometry.
   b. Discretize the model fault uniformly into N_0 dislocations.
   c. Discretize the data space uniformly into $K \times N_0$ data cells.
2. Model-space discretization
   a. Iterate through $i = 0$ to N model dislocations, and for each one:
      1. Replace that dislocation with a set of four equal-size dislocations.
      2. Recalculate a new elastic kernel, G.
      3. Compute CN, and record i for which CN is the smallest.
   b. Form a new model space by replacing the ith dislocation corresponding to the smallest CN by four equal-size dislocations, update $N = N + 3$, and proceed to step 3.
3. Data-space discretization
   a. Iterate through $j = 1$ to M data cells, and for each one:
      1. Replace that cell with a set of four equal-size data cells.
      2. Recalculate a new elastic kernel, G.
      3. Compute and store CN(j).
   b. Extract the subset of K data points corresponding to the K smallest CN, form a new dataset by replacing each of the K data points by four new data points obtained through a quad-division, and update the current number of data points: $M = M + 3K$.
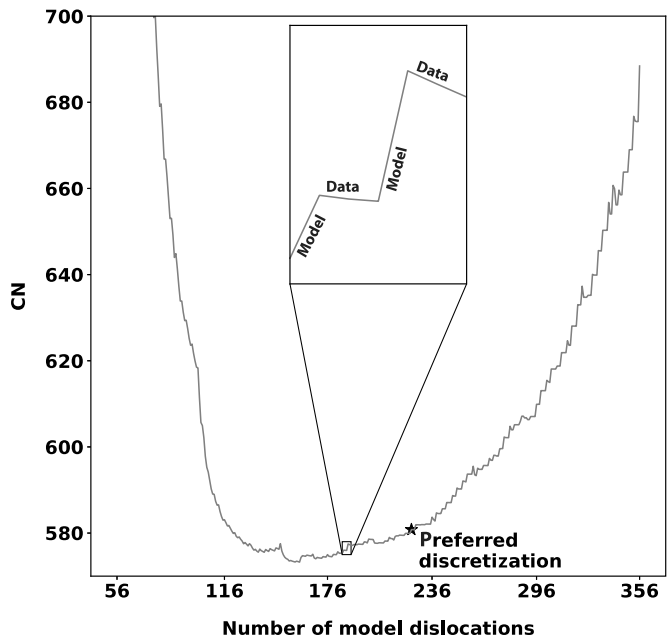   c. Return to step 2 or exit if the number of dislocations has reached a predetermined number.

Figure 6. The CN as a function of model dislocations (with a fixed 1:20 ratio between model dislocations to data points). Model-space discretization (step 2 of the discretization algorithm) results in CN increase, and data-space discretization (step 3 of the algorithm) results in CN decrease (figure inset). The star indicates the preferred discretization.

Results presented in this study are obtained using $N_0 = 56$, $K = 25$, and the minimum dislocation and data cell dimensions of 1.0 and 0.8 km, respectively. The evolution of CN with the number of model dislocations is shown in Figure 6. The CN increases during intervals of model discretization and decreases during intervals of data discretization (Fig. 6, inset). Initially, the decrease in CN due to data discretization is more pronounced than the increase, due to model discretization. Later, this situation changes, and the effect of model discretization overtakes. As a result, the evolution of CN is of U-shape, with a rather flat minimum extending from 125 to 225 dislocations, beyond which CN rises steeply. Our preferred discretization is located at the right side corner of the U-shape curve (indicated by the star in Fig. 6), which guarantees the most detailed, yet trustworthy view of the slip distribution. For example, it is shown that the CN of G (equation 1) corresponding to a fault model that is discretized as in Ross et al. (2019), as well as data that are downsampled proportionally to the displacement variance (Jónsson et al., 2002; Simons et al., 2002), is by a factor of 30 larger than that resulting from the model-data discretization introduced in this study. This CN improvement results in a factor of 1.8–2 reduction of the L2-norm discrepancy between true and modeled slip distributions (Table A1; Figs. A2–A5). Thus, optimizing the CN of inverse problems is an effective technique for reducing the effect of noise and analysis errors.
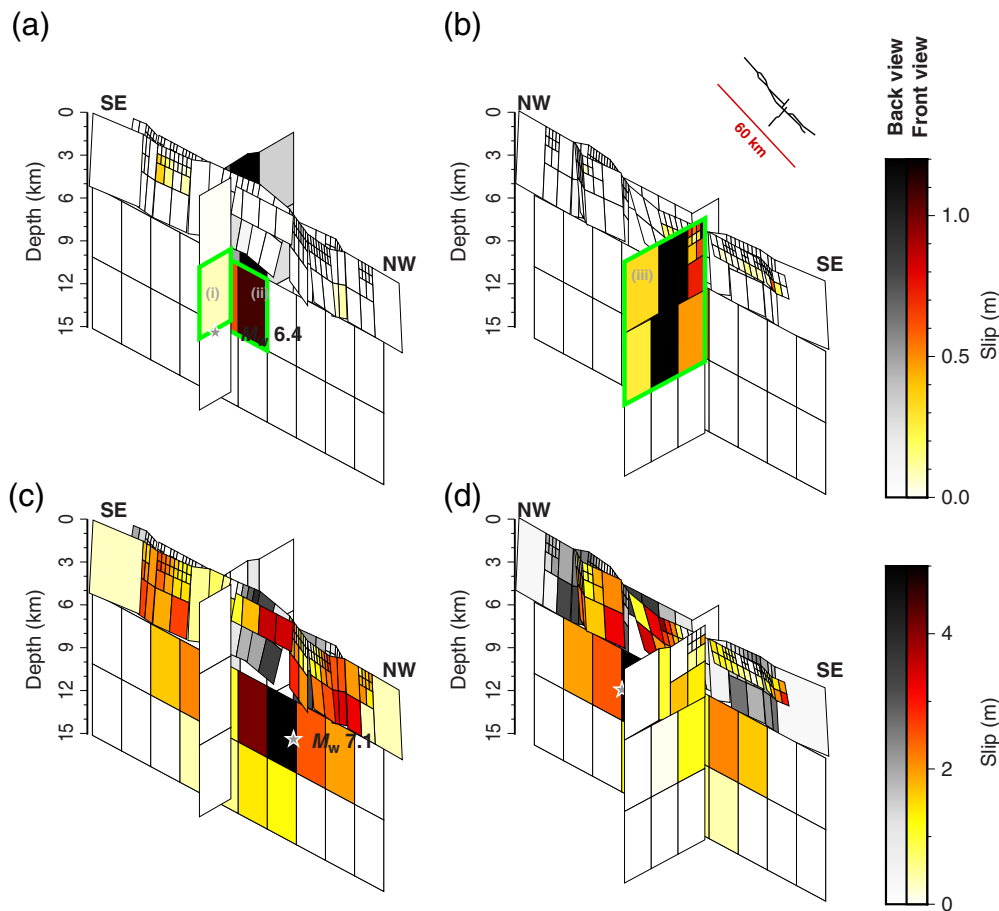
Figure 7. The preferred foreshock and mainshock slip models. (a,b) Different views of the foreshock slip distributions. (c,d) Different views of the mainshock slip distributions. Stars indicate the hypocenter locations. Three rectangles indicate the foreshock's asperities discussed in the Mechanical Implications of Fault Rerupture section. Whereas the coseismic slip of the foreshock was complex, involving three distinct asperities distributed among an intersecting orthogonal set of faults, the coseismic slip of the mainshock was limited to the main NW-striking fault. Also, note the repeat rupture of asperity II. SE, southeast. The color version of this figure is available only in the electronic edition.

SLIP MODELS

The foreshock and mainshock slip distributions are shown in Figure 7a,b and 7c,d, respectively. Modeled and observed GPS vectors are shown in Figure 1 (see also Tables A2–A5). Modeled and observed across-fault surface offsets are compared in Figure 8. Modeled, observed, and residual InSAR line of sight and optical imagery maps are presented in Figure 9. The L2-norm discrepancy between the modeled and observed sparse data is 5%, and that of the dense dataset is about 20% (Figs. 1 and 8).

In agreement with seismological estimates, the foreshock geodetic moment is equivalent to M_w 6.4, with most of the slip located at depth between 0 and 6 km on the northeast-striking segment, just south of its intersection with the northwest-striking faults. This asperity (labeled III in Fig. 7b) is responsible for 46% of the foreshock's geodetic moment. An additional 39% of the geodetic moment was released at depth between 6 and 12 km

on the main northwest-striking fault (labeled II in Fig. 7a). The remaining moment was released on a northeast-striking segment just north of the intersection with the northwest-striking faults (labeled I in Fig. 7a). Thus, the picture that emerges is of a complex rupture that ruptured orthogonal faults and propagated both laterally and vertically. The slip on asperity II triggered a large number of aftershocks on the northwest-striking segments, some of which occurred very close to the future site of the mainshock. Likewise, the slip on asperities I and III triggered aftershocks on the northeast-striking fault.

The mainshock geodetic moment is equivalent to M_w 7.0, about 0.1 magnitude units below the seismological estimates (Fig. 7c,d). About 98% of its geodetic moment has been released on the northwest-striking faults in two main asperities. The first is located southeast of the hypocenter at depth between 6 and 12 km, and the second is partitioned among three subparallel shallow branches of the deeper segment (upper 6 km) that are well resolved by InSAR, optical data, and field observations

(Brandenberg *et al.*, 2019). Interestingly, our model indicates that asperity II that ruptured during the foreshock slip has reruptured during the mainshock. The mechanical implication of this repeated failure within 34 hr is discussed in the Mechanical Implications of Fault Rerupture section.

STRESS TRANSFER DUE TO THE M_w 6.4 FORESHOCK

The spatiotemporal clustering of the Ridgecrest earthquake pair indicates a causal relationship between the two events. Here, we assess the possibility that the rupture of the M_w 7.1 earthquake has been promoted by the static stress change imparted by the M_w 6.4 earthquake. Static stress changes are calculated at the midpoint of each of the mainshock dislocations, using the isotropic homogeneous half-space formulation of Okada (1992). Following a common practice, we consider the Coulomb failure function (FF) to assess the
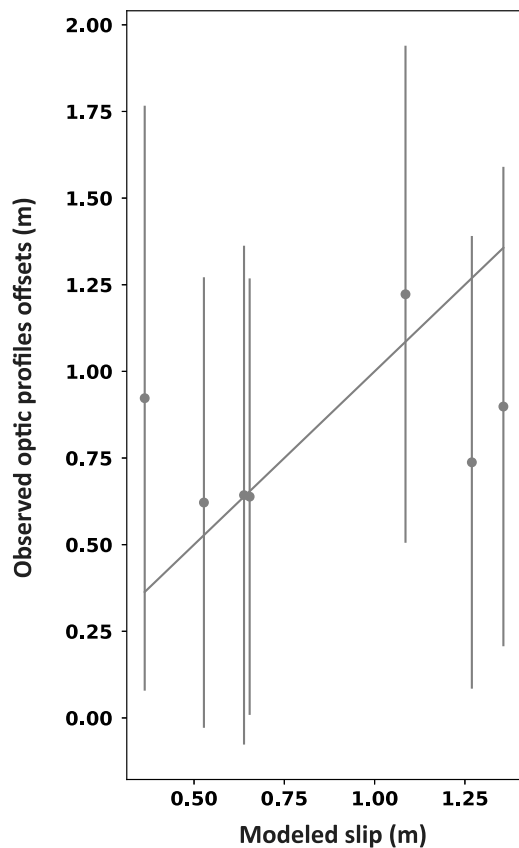
Figure 8. Observed versus modeled foreshock surface offsets inferred from optical imagery. The dashed line indicates a 1:1 ratio.

combined effect of shear and normal stress changes on receiver faults: $\Delta\sigma_{\mathrm{FF}} = \Delta\tau - \mu\Delta\sigma$, in which $\Delta\tau$ is the shear stress change (positive in the direction of slip), $\Delta\sigma$ is the change in effective normal stress (positive under compression), and μ is the coefficient of static friction (King *et al.*, 1994). Changes in the shear, normal, and Coulomb FF using $\mu = 0.6$ are presented in Figure 10a–c. We find that the effect of the foreshock is to increase the shear stress at the site of the mainshock by ∼0.6 MPa. About 90% of this increase is due to right-lateral foreshock slip on asperity II (Fig. 7b), sharing the same northwest-striking fault as the mainshock hypocenter. In addition, we obtain ∼0.02 MPa reduction in normal compression, resulting primarily from left-lateral foreshock slip on the northeast-striking faults (asperities I and II in Fig. 7a). Thus, we infer that the interaction between the foreshock and mainshock is dominated by shear stress changes due to slip on asperity II, and it is nearly insensitive to the static friction coefficient.
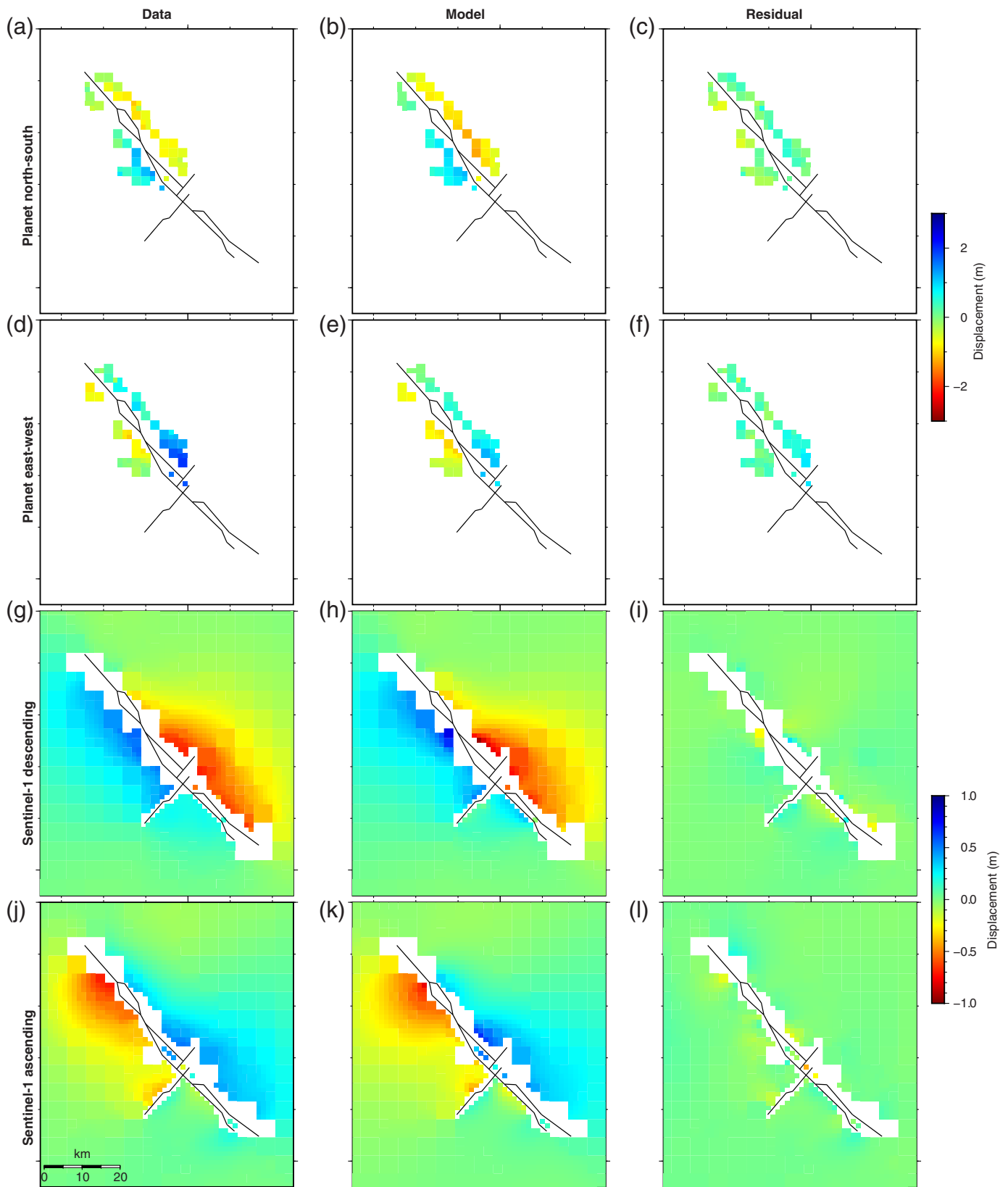
The results of the stress transfer analysis reported earlier are at odds with those of Barnhart *et al.* (2019), who obtained an order of magnitude smaller shear stress change. They further inferred a similar triggering effect for the M_{w} 6.4 foreshock and M_{w} 5.4 foreshock that ruptured 11 hr before the mainshock

just a few kilometers away from its hypocenter. Differences between their stress transfer analyses and ours are due to differences in the foreshock modeling approach. In their slip inversion, the foreshock is constrained to a single rupture plane, and consequently no foreshock slip is occurring on the northwest-striking fault. Although viewing the M_{w} 6.4 as the sole foreshock of the M_{w} 7.1 earthquake is a rather simplistic view of the triggering process, our analysis clearly shows that this interaction is dominated by shear stress change due to slip on asperity II. This stress change triggered smaller foreshocks, many of which occurred on the northwest-striking fault and may have further promoted the mainshock failure.

MECHANICAL IMPLICATIONS OF FAULT RERUPTURE

Our joint inversion of InSAR, GPS, and optical imagery very clearly indicates that the foreshock ruptured an orthogonal fault system with three main asperities, as detailed in the Slip Model section. The spatial extent and moment budget of these asperities are in general agreement with those inferred by Ross *et al.* (2019) on the basis of kinematic subevent inversion. Similar to their study, we infer that most of the foreshock seismic moment has been released on the northeast fault, south of the intersection point and at shallow depth (asperity III in Fig. 7b). This result is also in general agreement with the Ridgecrest foreshock static slip obtained via kinematic modeling of GPS and teleseismic data by Liu *et al.* (2019). The main disparity between our slip model and that of Ross *et al.* (2019) concerns the location of the orthogonal asperity (asperity II in Fig. 7a). Based on proximity to the hypocenter of the first subevent, Ross *et al.* (2019) placed this subevent on a secondary northwest-striking fault segment that is located 2–3 km to the north of the main northwest-striking fault. The optical imagery used in this study, however, very clearly rules out the possibility of shallow slip on this segment. At depths greater than 5 km, that segment merges with asperity II of the main fault (Ross *et al.*, 2019). The consequences of not allowing foreshock slip on asperity II leads to migration of slip from the main northwest-striking fault toward the secondary shallow northwest-striking segment. This, in turn, results in more than 20% data misfit increase, especially for the foreshock optical imagery. Furthermore, our stability analysis tests (see the Appendix) confirms that slip on asperity II is well resolved. We thus conclude that asperity II slipped during the foreshock rupture.
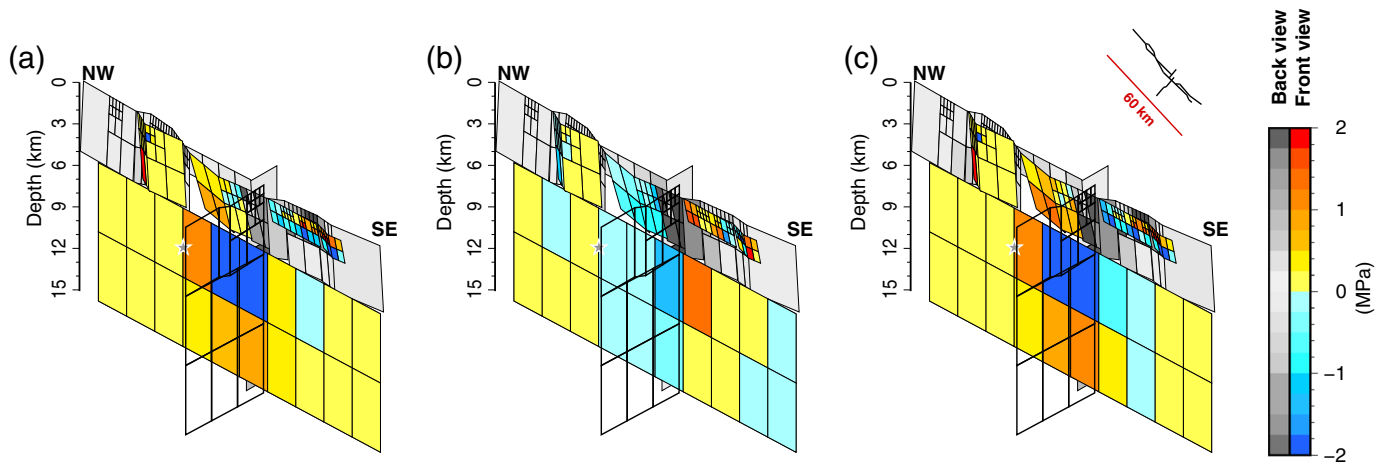
Although the foreshock rupture exhibits complex slip history, with three distinct asperities distributed among an intersecting orthogonal set of faults, the mainshock rupture has been limited to the main northwest-striking fault (see the Slip Model section). Its main asperity contains asperity II of the foreshock. That fault patch slipped up to 0.8 m during the foreshock, and it slipped up to 5 m about 34 hr later during the mainshock. We conclude that the rerupture on these model dislocations is a very robust attribute of the slip distribution; it

Figure 9. Observed (left), modeled (middle), and observed minus modeled residuals (right). (a–f) Planet pixel tracking offsets enclosing the times of the mainshock. (g–l) InSAR line of sight enclosing the times of the foreshock and mainshock. The color version of this figure is available only in the electronic edition.

is independent of the degree of smoothing, and it is essential for fitting the near-fault optical imagery data.

The rerupturing of asperity II has some interesting mechanical implications that we now discuss. Not only did asperity II fail

Figure 10. Stress changes imparted by the foreshock on NW-striking faults. (a) Shear stress; (b) normal stress; (c) Coulomb failure function, with a coefficient of friction equals 0.6. Stress changes are calculated at the midpoint of each model dislocation. The star indicates the location of the mainshock hypocenter. Note that the foreshock induced a 0.6 MPa shear stress increase at the site of the mainshock. The color version of this figure is available only in the electronic edition.

twice within a very short interval, but it also slipped about six times more during the mainshock than during the foreshock rupture. Furthermore, asperity II is where the mainshock slip is the largest. This observation indicates that the stress drop during the foreshock released a small fraction of the tectonic loading. Repeating slip of fault patches during individual earthquakes were reported in the past; for example, this happened during the 1987 Superstition Hills (Wald *et al.*, 1990), the 1999 Chi Chi (Lee *et al.*, 2006), and the 2011 Tohoku-Oki (Lee *et al.*, 2011) earthquakes. Reruptures are also reproduced in stick-slip laboratory experiments (Nielsen *et al.*, 2000). What is unique here is that these fault patches ceased to slip for about 34 hr. That this fault patch ceased to slip, despite a drop of just a small fraction of the driving stresses, requires an efficient dynamic strength recovery mechanism, such as those inferred from kinematic slip models (Heaton, 1990) or reported in laboratory friction experiments (e.g., Shimamoto, 1986; Kilgore *et al.*, 1993; Weeks, 1993). Numerical simulations of frictional sliding indicate that partial stress drops are in fact the consequence of dynamic strengthening and that the latter results from highly rate-dependent friction (Madariaga and Cochard, 1996). Finally, strongly rate-dependent friction is thought to promote self-healing slip pulses (e.g., Heaton, 1990; Perrin *et al.*, 1995; Madariaga and Cochard, 1996; Zheng and Rice, 1998; Gabriel *et al.*, 2012), a behavior that has been inferred by Chen *et al.* (2020) on the basis of kinematic inversions of the Ridgecrest mainshock.

SUMMARY

We obtained distinct slip distributions for the M_w 7.1 Ridgecrest and its M_w 6.4 foreshock via joint inversion of InSAR, GPS, and optical imagery measurements. In setting-up the joint slip inversion, we implemented a new approach for data and model discretization that stabilizes the inversion, preventing small changes in the data space from causing large changes to the model space. We find that whereas the coseismic slip of the M_w 6.4 earthquake was complex, with three distinct asperities distributed among an intersecting orthogonal set of faults, the coseismic slip of the M_w 7.1 earthquake was limited to the main northwest-striking fault. We draw attention to a fault asperity

that slipped twice within about 34 hr. When it slipped for the first time during the foreshock rupture, it increased the shear stress at the site of the future mainshock hypocenter and raised the seismicity rate on the main northwest-striking fault. In addition to failing twice within a short interval, the reruptured asperity slipped five to six times more during the mainshock than during the foreshock. We note that such a fault rerupturing is indicative of a partial stress drop during the foreshock and that the premature slip arrest under such conditions requires an efficient frictional strengthening. We emphasize the causal link between highly rate-dependent friction, dynamic frictional restrengthening, and partial stress drop observed in numerical studies of frictional sliding. These mechanical aspects are at the core of earthquake science, as they may hold the key to understanding fault-slip complexity (Madariaga and Cochard, 1996).

DATA AND RESOURCES

Interferometric Synthetic Aperture Radar (InSAR) data are from Sentinel-1 European Space Agency (ESA) Single Look Complex (SLC) Synthetic Aperture Radar (SAR) data freely available at https://scihub.copernicus.eu/dhus/#/home and were processed by Gamma remote sensing software. Global Positioning System (GPS) displacement data are from the Nevada Geodetic Laboratory rapid 5 min solutions, which are publicly available at http://geodesy.unr.edu/news_items/20190707/ci38457511_forweb.txt for the mainshock and http://geodesy.unr.edu/news_items/20190705/ci38443183_forweb.txt for the foreshock. Planet imagery is provided courtesy of Planet Labs, Inc. Active fault locations were extracted from the U.S. Geological Survey (USGS) Quaternary Fault and Fold Database of the United States (https://earthquake.usgs.gov/hazards/qfaults/). Plots were made using the Generic Mapping Tools v.5 available at https://www.generic-mapping-tools.org/ (Wessel *et al.*, 2013). All websites were last accessed in January 2020.

REFERENCES

Barnhart, W. D., G. P. Hayes, and R. D. Gold (2019). The July 2019 Ridgecrest, California, earthquake sequence: Kinematics of slip and stressing in cross-fault ruptures, *Geophys. Res. Lett.* **46,** doi: 10.1029/2019GL084741.

Blewitt, G., W. Hammond, and C. Kreemer (2018). Harnessing the GPS data explosion for interdisciplinary science, *Eos* **99,** doi: 10.1029/2018eo104623.

Brandenberg, S. J., P. Wang, C. C. Nweke, K. Hudson, S. Mazzoni, Y. Bozorgnia, W. K. Hudnut, A. C. Davis, K. S. Ahdi, F. Zareian, *et al.* (2019). *Preliminary Report on Engineering and Geological Effects of the July 2019 Ridgecrest Earthquake Sequence*, J. P. Stewart (Editor), doi: 10.18118/G6H66K.

Chen, K., J.-P. Avouac, S. Aati, C. Milliner, F. Zheng, and C. Shi (2020). Cascading and pulse-like ruptures during the 2019 Ridgecrest earthquakes in the Eastern California Shear Zone, *Nat. Comm.* **11,** no. 1, 22, doi: 10.1038/s41467-019-13750-w.

Costantini, M., and P. A. Rosen (1999). A generalized phase unwrapping approach for sparse data, *IEEE 1999 International Geoscience and Remote Sensing Symposium. IGARSS'99*, Cat. No. 99CH36293, Vol. 1, 267–269, doi: 10.1109/IGARSS.1999.773467.

Curtis, A., and R. Snieder (1997). Reconditioning inverse problems using the genetic algorithm and revised parameterization, *Geophysics* **62,** no. 4, 1524–1532, doi: 10.1190/1.1444255.

Fukuyama, E. (1991). Inversion for the rupture details of the 1987 east Chiba earthquake, Japan, using a fault model based on the distribution of relocated aftershocks, *J. Geophys. Res.* **96,** doi: 10.1029/91JB00328.

Fukuyama, E. (2015). Dynamic faulting on a conjugate fault system detected by near-fault tilt measurements, *Earth Planets Space* **67,** doi: 10.1186/s40623-015-0207-1.

Gabriel, A. A., J. P. Ampuero, L. A. Dalguer, and P. M. Mai (2012). The transition of dynamic rupture styles in elastic media under velocity-weakening friction, *J. Geophys. Res.* **117,** doi: 10.1029/2012JB009468.

Gallovic, F., and J. P. Ampuero (2015). A new strategy to compare inverted rupture models exploiting the eigenstructure of the inverse problem, *Seismol. Res. Lett.* **86,** doi: 10.1785/0220150096.

Goldstein, R. M., and C. L. Werner (1998). Radar interferogram filtering for geophysical applications, *Geophys. Res. Lett.* **25,** doi: 10.1029/1998GL900033.

Hauksson, E., W. Yang, and P. M. Shearer (2012). Waveform relocated earthquake catalog for Southern California (1981 to June 2011), *Bull. Seismol. Soc. Am.* **102,** doi: 10.1785/0120120010.

Heaton, T. H. (1990). Evidence for and implications of self-healing pulses of slip in earthquake rupture, *Phys. Earth Planet. In.* **64,** doi: 10.1016/0031-9201(90)90002-F.

Hudnut, K. W., L. Seeber, and J. Pacheco (1989). Cross-fault triggering in the November 1987 Superstition Hills earthquake sequence, southern California, *Geophys. Res. Lett.* **16,** doi: 10.1029/GL016i002p00199.

Jennings, C. W., and W. A. Bryant (2010). 2010 fault activity map of California, *Geologic Data Map No. 6*, California Geological Survey, Sacramento, California, Scale 1:750,000.

Jónsson, S., H. Zebker, P. Segall, and F. Amelung (2002). Fault slip distribution of the 1999 Mw 7.1 Hector Mine, California, earthquake, estimated from satellite radar and GPS measurements, *Bull. Seismol. Soc. Am.* **92,** no. 4, 1377–1389, doi: 10.1785/0120000922.

Kilgore, B. D., M. L. Blanpied, and J. H. Dieterich (1993). Velocity dependent friction of granite over a wide range of conditions, *Geophys. Res. Lett.* **20,** doi: 10.1029/93GL00368.

King, G. C. P., R. S. Stein, and J. Lin (1994). Static stress changes and the triggering of earthquakes, *Bull. Seismol. Soc. Am.* **84,** no. 3, 935–953.

Krabbenhoeft, A., R. von Huene, J. J. Miller, D. Lange, and F. Vera (2018). Strike-slip 23 January 2018 M_W 7.9 Gulf of Alaska rare intraplate earthquake: Complex rupture of a fracture zone system. *Sci. Rep.* **8,** doi: 10.1038/s41598-018-32071-4.

Larsen, S., R. Reilinger, H. Neugebauer, and W. Strange (1992). Global positioning system measurements of deformations associated with the 1987 Superstition Hills earthquake: Evidence for conjugate faulting, *J. Geophys. Res.*, doi: 10.1029/92JB00128.

Lawson, C. L., and R. J. Hanson (1974). Solving least-squares problems, in *Solving Least-Squares Problems*, doi: 10.1137/1.9781611971217.

Lee, S. J., B. S. Huang, M. Ando, H. C. Chiu, and J. H. Wang (2011). Evidence of large scale repeating slip during the 2011 Tohoku-Oki earthquake, *Geophys. Res. Lett.* **38,** doi: 10.1029/2011GL049580.

Lee, S. J., K. F. Ma, and H. W. Chen (2006). Three-dimensional dense strong motion waveform inversion for the rupture process of the 1999 Chi-Chi, Taiwan, earthquake, *J. Geophys. Res.* **111,** doi: 10.1029/2005JB004097.

Leprince, S., F. Ayoub, Y. Klinger, and J. Avouac (2007). Co-registration of optically sensed images and correlation (COSI-Corr): An operational methodology for ground deformation measurements, *2007 IEEE International Geoscience and Remote Sensing Symposium*, 1943–1946, doi: 10.1109/IGARSS.2007.4423207.

Lin, G., P. M. Shearer, and E. Hauksson (2007). Applying a three-dimensional velocity model, waveform cross correlation, and cluster analysis to locate southern California seismicity from 1981 to 2005, *J. Geophys. Res.* **112,** doi: 10.1029/2007JB004986.

Liu, C., T. Lay, E. E. Brodsky, K. Dascher-Cousineau, and X. Xiong (2019). Coseismic rupture process of the large 2019 Ridgecrest earthquakes from joint inversion of geodetic and seismological observations, *Geophys. Res. Lett.* **46,** doi: 10.1029/2019GL084949.

Madariaga, R., and A. Cochard (1996). Dynamic friction and the origin of the complexity of earthquake sources, *Proc. Natl. Acad. Sci. Unit. States Am.* **93,** doi: 10.1073/pnas.93.9.3819.

Meng, L., J. P. Ampuero, J. Stock, Z. Duputel, Y. Luo, and V. C. Tsai (2012). Earthquake in a maze: Compressional rupture branching during the 2012 M_w 8.6 Sumatra earthquake, *Science* **337,** doi: 10.1126/science.1224030.

Nielsen, S. B., J. M. Carlson, and K. B. Olsen (2000). Influence of friction and fault geometry on earthquake rupture, *J. Geophys. Res.* **105,** doi: 10.1029/1999jb900350.

Okada, Y. (1985). Surface deformation due to shear and tensile faults in a half-space Okada, Y Bull Seismol Soc AmV75, N4, Aug 1985, P1135–1154, *Int. J. Rock Mech. Min. Sci. Geomech. Abstr.* **75,** 1135–1154, doi: 10.1016/0148-9062(86)90674-1.

Okada, Y. (1992). Internal deformation due to shear and tensile faults in a half-space, *Bull. Seismol. Soc. Am.* **82,** no. 2, 1018–1040.

Page, M. T., S. Custódio, R. J. Archuleta, and J. M. Carlson (2009). Constraining earthquake source inversions with GPS data: 1. Resolution-based removal of artifacts, *J. Geophys. Res.* **114,** doi: 10.1029/2007JB005449.

Perrin, G., J. R. Rice, and G. Zheng (1995). Self-healing slip pulse on a frictional surface, *J. Mech. Phys. Solids* **43,** doi: 10.1016/0022-5096 (95)00036-I.

Ross, Z. E., B. Idini, Z. Jia, O. L. Stephenson, M. Zhong, X. Wang, Z. Zhan, M. Simons, J. E. Fielding, S. Yum, *et al.* (2019). Hierarchical interlocked orthogonal faulting in the 2019 Ridgecrest earthquake sequence, *Science* **366,** doi: 10.1126/science.aaz0109.

Ruppert, N. A., C. Rollins, A. Zhang, L. Meng, S. G. Holtkamp, M. E. West, and J. T. Freymueller (2018). Complex faulting and triggered rupture during the 2018 M_W 7.9 Offshore Kodiak, Alaska, earthquake, *Geophys. Res. Lett.* **45,** doi: 10.1029/2018GL078931.

Shimamoto, T. (1986). Transition between frictional slip and ductile flow for halite shear zones at room temperature, *Science* **231,** doi: 10.1126/science.231.4739.711.

Simons, M., Y. Fialko, and L. Rivera (2002). Coseismic deformation from the 1999 Mw 7.1 Hector Mine, California, earthquake as inferred from InSAR and GPS observations, *Bull. Seismol. Soc. Am.* **92,** no. 4, 1390–1402, doi: 10.1785/0120000933.

Wald, D. J., D. V. Helmberger, and S. H. Hartzell (1990). Rupture process of the 1987 Superstition Hills earthquake from the inversion of strong-motion data, *Bull. Seismol. Soc. Am* **80,** no. 5, 1079–1098.

Weeks, J. D. (1993). Constitutive laws for high-velocity frictional sliding and their influence on stress drop during unstable slip, *J. Geophys. Res.* **98,** no. B10, 17,637.

Wegmuller, U., C. Werner, and T. Strozzi (1998). SAR interferometric and differential interferometric processing chain, *IGARSS '98. Sensing and Managing the Environment. 1998 IEEE International Geoscience and Remote Sensing. Symposium Proceedings*, Cat. No. 98CH36174, Vol. 2, 1106–1108, doi: 10.1109/IGARSS.1998.699687.

Wessel, P., W. H. F. Smith, R. Scharroo, J. Luis, and F. Wobbe (2013). Generic mapping tools: Improved version released, *Eos Trans. AGU*, doi: 10.1002/2013EO450001.

Yue, H., T. Lay, and K. D. Koper (2012). En échelon and orthogonal fault ruptures of the 11 April 2012 great intraplate earthquakes, *Nature* **490,** doi: 10.1038/nature11492.

Zheng, G., and J. R. Rice (1998). Conditions under which velocity-weakening friction allows a self-healing versus a cracklike mode of rupture, *Bull. Seismol. Soc. Am.* **88,** no. 6, 1466–1483.

Zinke, R., J. Hollingsworth, J. F. Dolan, and R. Van Dissen (2019). Three-dimensional surface deformation in the 2016 MW 7.8 Kaikōura, New Zealand, earthquake from optical image correlation: Implications for strain localization and long-term evolution

of the Pacific-Australian plate boundary, *Geochem. Geophys. Geosys.* **20,** doi: 10.1029/2018GC007951.

Ziv, A. (2016). Reconditioning fault slip inversions via InSAR data discretization, *J. Seismol.* **20,** no. 4, 1123–1129, doi: 10.1007/ s10950-016-9558-8.

APPENDIX

Model sensitivity to noisy data and analysis errors

The sensitivity of the fully reconditioned (data and model) inversion to small changes in the data space is
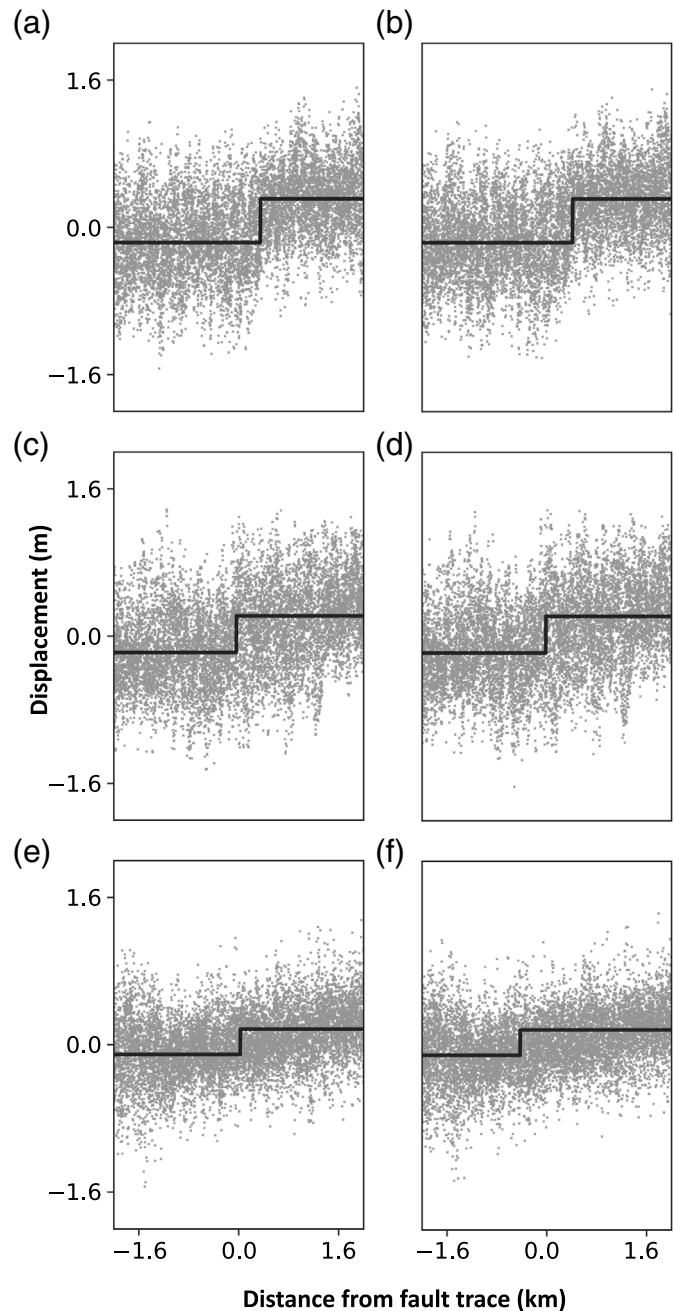

Figure A1. Enlarged view of displacement profiles in Figure 5. (a,c,e) East–west profiles; (b,d,f) north–south profiles. Profile locations are shown in Figure 4. Black lines are least-square fits to a step function.

assessed numerically as in Ziv (2016). The test follows these steps:

1. simulate noise-free Interferometric Synthetic Aperture Radar (InSAR) and optical imagery maps from a predetermined slip model;
2. obtain InSAR noise-only maps using randomly generated numbers;
3. generate noisy InSAR and optical imagery maps by adding the products of step 1 and 2 earlier;
4. solve for the slip distribution using the nonnegative algorithm of Lawson and Hanson (1974); and
5. repeat steps 1–4 1000 times and for each dislocation comprising the model fault, record the standard deviation of the discrepancies between the true and modeled slips.

The results of four such tests that differ in their noise and/or slip attributes as detailed in Table A1 are summarized in Figures A2–A5. Inspection of the standard deviation of the slip discrepancies reveals notable reduction in the slip discrepancy
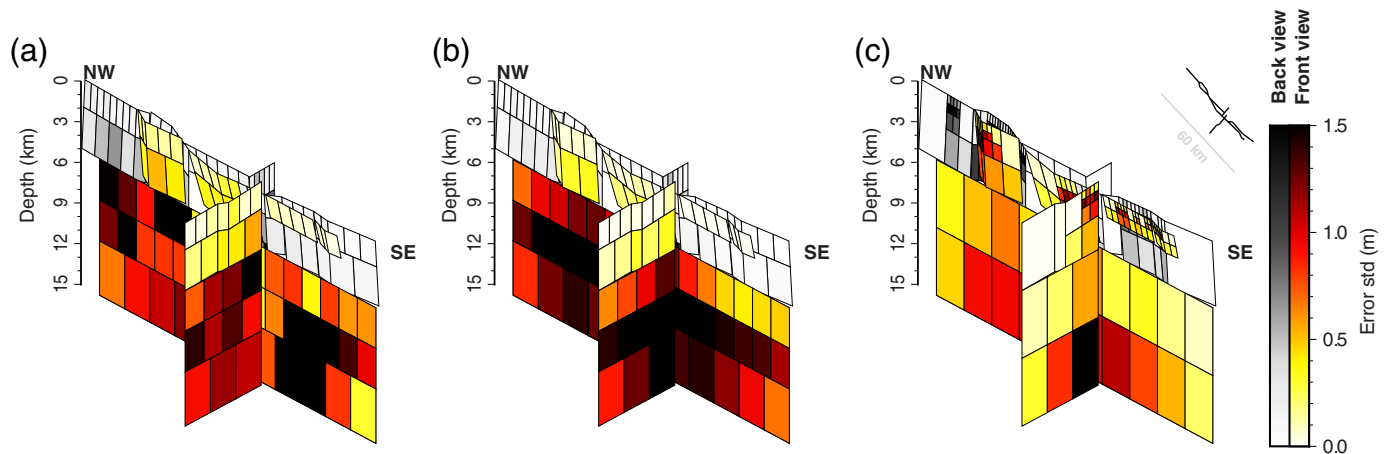

Figure A2. Results of sensitivity test 1. This test uses uniform input slip of 1 m and spatially uncorrelated randomly distributed noise with 0 mean and standard deviation of 0.5 and 5 cm for the Interferometric Synthetic Aperture Radar (InSAR) and optic datasets, respectively. The standard deviations of 1000 slip inversions are shown for the following discretization approaches: (a) data sampled uniformly; (b) data sampled according to displacement variance; and (c) fully reconditioned data and model spaces. The standard deviation weighted sums are reported in Table A1. NW, northwest; SE, southeast. The color version of this figure is available only in the electronic edition.

Figure A3. Results of sensitivity test 2. This test uses uniform input slip of 1 m and spatially correlated noise with a maximum amplitude of 1 and 10 cm for the InSAR and optic data, respectively. The standard deviations of 1000 slip inversions are shown for the following discretization approaches: (a) data sampled uniformly; (b) data sampled according to displacement variance; and (c) fully reconditioned data and model spaces. The standard deviation weighted sums are reported in Table A1. The color version of this figure is available only in the electronic edition.
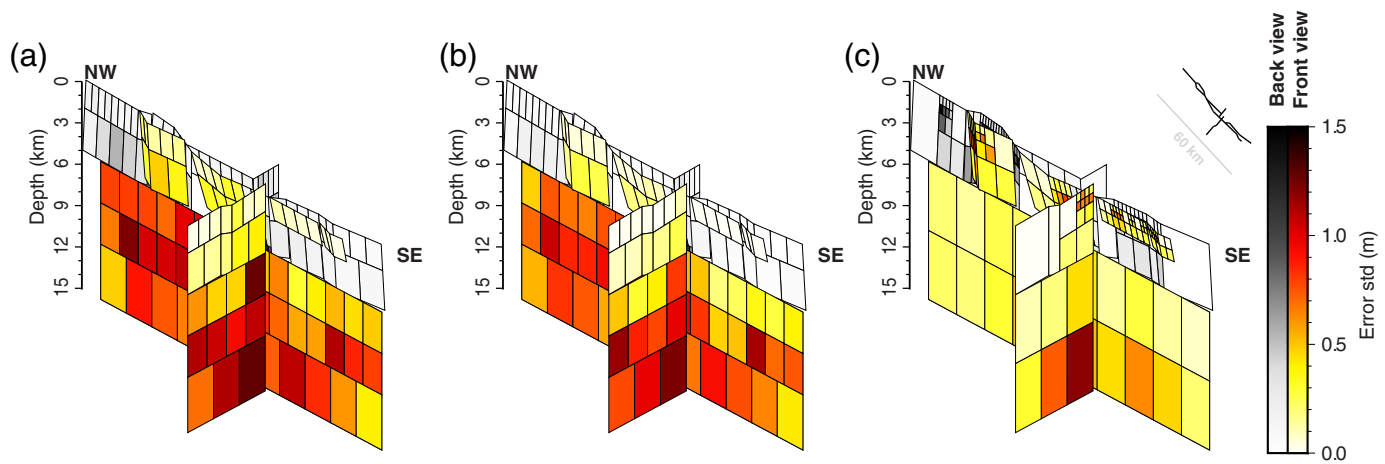
Figure A4. Results of sensitivity test 3. This test uses randomly distributed slip between 0 and 1 m and spatially uncorrelated randomly distributed noise with 0 mean and standard deviation of 0.5 and 5 cm for the InSAR and optic datasets, respectively. The standard deviations of 1000 slip inversions are shown for the following discretization approaches: (a) data sampled uniformly; (b) data sampled according to displacement variance; and (c) fully reconditioned data and model spaces. The standard deviation weighted sums are reported in Table A1. The color version of this figure is available only in the electronic edition.

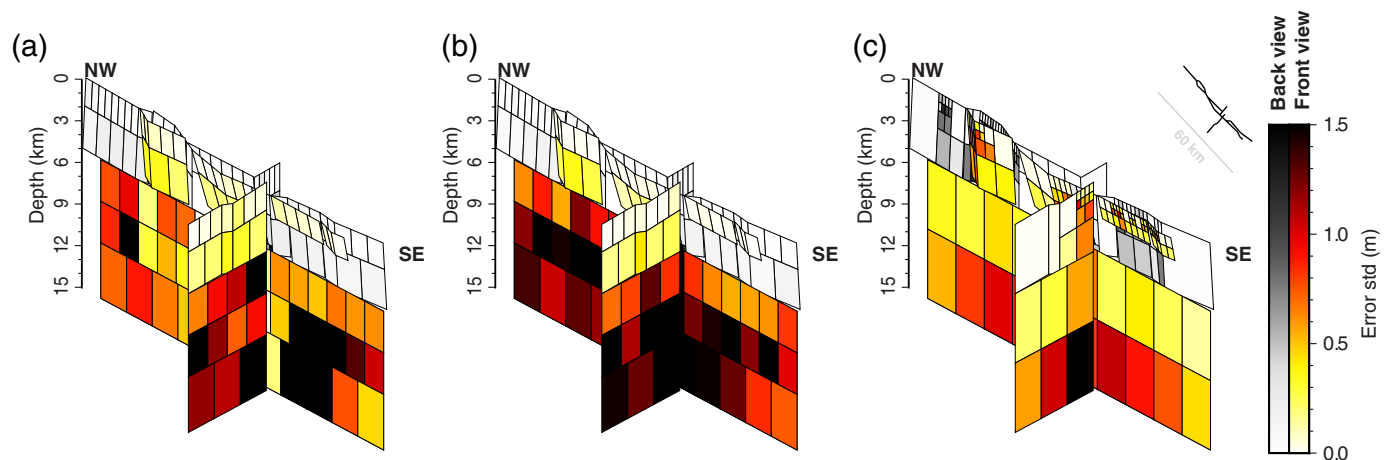**Figure A5.** Results of sensitivity test 4. This test uses randomly distributed slip between 0 and 1 m and spatially correlated noise with a maximum amplitude of 1 and 10 cm for the InSAR and optic data, respectively. The standard deviations of 1000 slip inversions are shown for the following discretization approaches: (a) data sampled uniformly; (b) data sampled according to displacement variance; and (c) fully reconditioned data and model spaces. The standard deviation weighted sums are reported in Table A1. The color version of this figure is available only in the electronic edition.
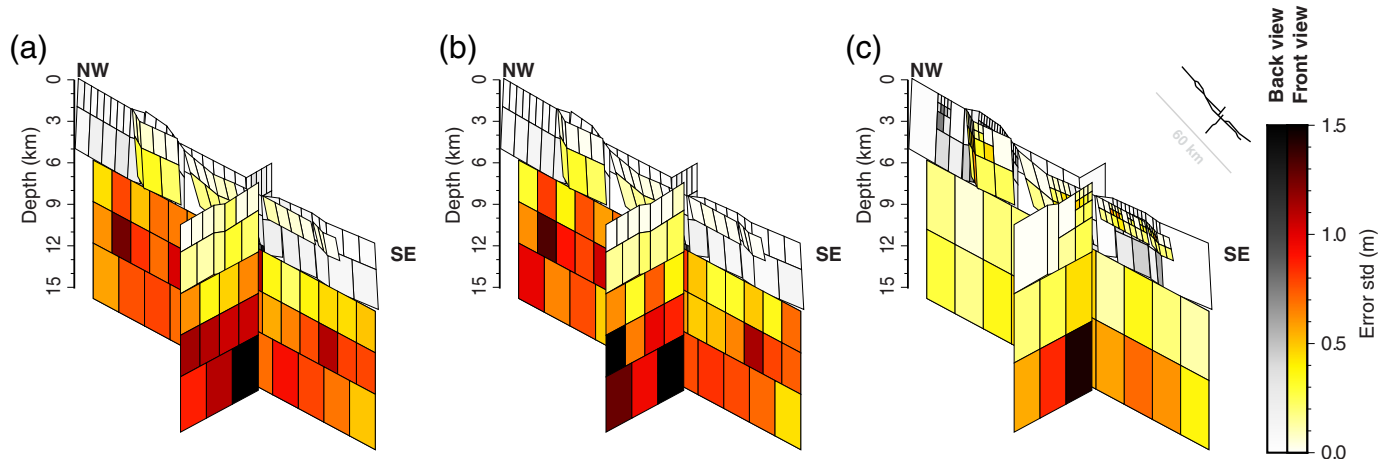
TABLE A1
A Summary for the Noise Sensitivity Tests

Data and Model Discretization Method	CN	WS Test 1	WS Test 2	WS Test 3	WS Test 4
Predefined model (as in Ross et al., 2019) and data sampled uniformly	22,306	0.805	0.627	0.552	0.495
Predefined model (as in Ross et al., 2019) and data sampled according to displacement variance	20,198	0.805	0.833	0.463	0.495
Fully reconditioned data and model spaces	599	0.493	0.487	0.309	0.319

The standard deviation weighted sum of each test is listed. These are calculated as follows: $\text{WS} = \sum_i \text{st.dev.}_i S_i / S$, in which st.dev.$_i$ and S_i are the standard deviation and area of the ith dislocation and S is the fault total area. Four different combinations of slip and noise models were examined. Test 1 uses uniform input slip of 1 m and spatially uncorrelated randomly distributed noise with 0 mean and standard deviation of 0.5 and 5 cm for the Interferometric Synthetic Aperture Radar (InSAR) and optic datasets, respectively. Test 2 uses uniform input slip of 1 m and spatially correlated noise with a maximum amplitude of 1 and 10 cm for the InSAR and optic data, respectively. Test 3 uses randomly distributed slip between 0 and 1 m and spatially uncorrelated randomly distributed noise with 0 mean and standard deviation of 0.5 and 5 cm for the InSAR and optic datasets, respectively. Finally, test 4 uses randomly distributed slip between 0 and 1 m and spatially correlated noise with a maximum amplitude of 1 and 10 cm for the InSAR and optic data, respectively. CN, condition number; WS, weighted sum.

TABLE A2
Global Positioning System (GPS) Sites Location and East–West Displacement Component of the 6 July 7.1 M_w Earthquake

ID	Longitude (°)	Latitude (°)	E	E_model	Se
P595	−117.4028	35.6976	0.51405	0.51729846	0.00037
CCCC	−117.6712	35.5653	−0.04983	−0.0477157	0.00038
P580	−117.1922	35.6209	0.19171	0.1960031	0.00037
P594	−117.3901	35.8967	0.06576	0.07472597	0.0004
BEPK	−118.0741	35.8784	−0.09892	−0.0968919	0.00045
P464	−117.41	36.159	−0.0235	−0.0102275	0.0004
RAMT	−117.6833	35.3387	0.00741	0.00769427	0.0004
WORG	−118.2424	35.6956	−0.05828	−0.0570128	0.0006
P597	−116.8884	35.7106	0.05366	0.06556091	0.00038
P570	−118.26	35.6673	−0.05173	−0.0517636	0.00039
DTPG	−117.8459	35.2675	0.00086	0.00288139	0.00037
WHFG	−118.352	35.6951	−0.04254	−0.0433555	0.0004
P616	−117.8933	35.4246	−0.01012	−0.0131672	0.00037
P592	−117.3032	35.2386	−0.00525	−0.0005407	0.00038
CPBN	−117.573	35.0717	−0.00298	0.00213358	0.00039
P590	−117.3648	35.1168	−0.00542	−0.000534	0.00037
P573	−118.2605	36.0931	−0.03435	−0.0289189	0.00038
WASG	−118.557	35.7384	−0.03432	−0.028792	0.00066
ISLK	−118.4743	35.6623	−0.03242	−0.0318958	0.00039

Observed (from the Nevada Geodetic Laboratory rapid 5 min solution, Blewitt et al., 2018, see Data and Resources) and modeled GPS displacements at stations within 85 km from the 6 July M_w 7.1 Ridgecrest earthquake. E, East; Se, East standard deviation.

TABLE A3
Global Positioning System (GPS) Sites North–South and Up–Down Displacement Components of the 6 July 7.1 M_w Earthquake

ID	N	N_model	Sn	Up	Up_model	Su
P595	−0.24984	−0.2531101	0.00045	0.04284	0.03312446	0.00142
CCCC	0.21314	0.20636302	0.00046	0.00253	0.0100217	0.00146
P580	−0.02267	−0.0190045	0.00045	−0.00603	−0.0222275	0.00141
P594	−0.12663	−0.1278861	0.00048	0.00516	0.00311288	0.00152
BEPK	0.01287	0.01145406	0.00054	−0.00807	−0.0190416	0.00171
P464	−0.09248	−0.0860833	0.00048	0.01692	0.01670438	0.00153
RAMT	0.08813	0.09116635	0.00048	0.00441	0.0170851	0.00153
WORG	−0.00189	0.00089379	0.00073	0.00041	−0.0133603	0.0023
P597	−0.00259	−0.0026006	0.00045	−0.00672	−0.0150578	0.00143
P570	0.00054	0.00047686	0.00048	−0.00576	−0.0122758	0.00151
DTPG	0.04374	0.04564561	0.00045	0.00829	0.00977216	0.00142
WHFG	0.0019	0.00081931	0.00048	−0.00518	−0.0110517	0.00153
P616	0.04124	0.04201516	0.00044	0.00076	0.00483729	0.0014
P592	0.04048	0.0504665	0.00046	0.00363	0.01078504	0.00146
CPBN	0.03753	0.04295499	0.00047	0.00978	0.01123501	0.00148
P590	0.03704	0.04196749	0.00045	0.00697	0.01043335	0.00142
P573	0.00808	0.00263959	0.00046	0.00245	−0.0069248	0.00145
WASG	−0.00233	0.00107076	0.00079	0.01183	−0.0081556	0.00251
ISLK	−0.00018	0.00044612	0.00047	0.00597	−0.0086639	0.00149

Observed (from the Nevada Geodetic Laboratory rapid 5 min solution, Blewitt et al., 2018, see Data and Resources) and modeled GPS displacements at stations within 85 km from the 6 July M_w 7.1 Ridgecrest earthquake. N, North; Sn, North standard deviation; Su, up standard deviation.

Global Positioning System (GPS) Sites Location and East–West Displacement Component of the 4 July 6.4 M_w Earthquake

ID	Longitude (°)	Latitude (°)	E	E_model	Se
P595	−117.4028	35.6976	0.10531	0.10579004	0.00065
CCCC	−117.6712	35.5653	−0.04284	−0.0422203	0.00067
P594	−117.3901	35.8967	−0.01008	−0.001561	0.00069
P580	−117.1922	35.6209	0.02252	0.02821208	0.00065
RAMT	−117.6833	35.3387	−0.00122	0.00141438	0.00073
DS13	−116.7915	35.2478	0.01226	0.00213691	0.00069
P616	−117.8933	35.4246	−0.00914	−0.0066263	0.00063
P464	−117.41	36.159	−0.00255	−0.0005578	0.0007
P592	−117.3032	35.2386	−0.00384	−0.0007318	0.00066

Observed (from the Nevada Geodetic Laboratory rapid 5 min solution, Blewitt *et al.*, 2018, see Data and Resources) and modeled GPS displacements at stations within 50 km from the 4 July M_w 6.4 Ridgecrest earthquake. E, East; Se, East standard deviation.

Global Positioning System (GPS) sites North–South and Up–Down Displacement Components of the 4 July 6.4 M_w Earthquake

ID	N	N_model	Sn	Up	Su	Up_model
P595	0.00344	0.00365963	0.00078	0.02432	0.00247	0.01859787
CCCC	0.00449	0.00369664	0.0008	0.01529	0.00254	0.00283782
P594	−0.02025	−0.0220671	0.00083	0.00157	0.00264	0.0014366
P580	−0.00212	−0.001432	0.00078	0.00013	0.00247	−0.0032298
RAMT	0.01826	0.01632092	0.00088	0.00315	0.0028	0.0023528
DS13	0.00506	0.00034595	0.00083	0.02036	0.00262	−0.0004278
P616	0.00341	0.00153387	0.00076	0.0016	0.00241	−0.0007596
P464	−0.00941	−0.00946	0.00085	0.0036	0.00268	0.00192316
P592	0.00865	0.00825235	0.0008	−0.00703	0.00253	0.0016458

Observed (from the Nevada Geodetic Laboratory rapid 5 min solution, Blewitt *et al.*, 2018, see Data and Resources) and modeled GPS displacements at stations within 50 km from the 4 July M_w 6.4 Ridgecrest earthquake. N, North; Sn, North standard deviation; Su, up standard deviation.

with decreasing condition number (CN). It is thus concluded that optimizing the CN of inverse problems is an effective technique for reducing the effect of noise and analysis errors and that the data-and-model reconditioning algorithm yields fault-slip distributions that are more stable and closer to the true slip distribution.

Global Positioning System model results

Tables A2–A5 provide the Global Positioning System (GPS) model results.